RESEARCH ARTICLE

PETROGRAPHY AND GEOCHEMISTRY OF SOME PALEOPROTEROZOIC GRANITOIDS AT THE NORTH-EASTERN MARGIN OF THE KUMASI BASIN IN GHANA

Blestmond A. Brako[a]*, Gordon Foli[1], Kofi Adomako-Ansah[b], Derrick Aikins[b], Solomon Dery[c], Simon K.Y. Gawu[a]

[a] Department of Geological Engineering, College of Engineering Kwame Nkrumah University of Science and Technology, Kumasi, Ghana.
[b] Department of Geological Engineering, University of Mines and Technology, Tarkwa, Ghana.
[c] Azumah Resources Ghana Limited, Nadowli, Upper-West Region, Ghana.
*Corresponding Author Email: bblestmond@gmail.com

ARTICLE DETAILS

ABSTRACT

This study investigates basin-type granitoid samples from the north-eastern margin of the Kumasi Basin in Ghana to establish their source and geodynamic setting. Petrographic analysis, TAS and A/NK-A/CNK plots classify the granitoids as metaluminous quartz diorite, metaluminous granodiorite, and peraluminous monzogranite; and exhibiting I-type signatures. These rocks are formed by magma differentiation and/or partial melting at various stages. Distribution patterns of incompatible elements and the positive Eu/Eu* anomalies of 1.15 and 1.47 exhibited by quartz diorite and granodiorite, respectively, the values suggest the rocks crystallized from melts formed in a water-saturated environment. The negative Eu/Eu* anomaly exhibited by monzogranite indicate fractionation of plagioclase in the final stages of the magma evolution. The water-rich environment is probably due to dewatering of the basin's foreland volcaniclastic sediments during regional subsidence, burial and metamorphism. K_2O enrichments and wide variations suggest that the granodiorite and monzogranite are formed from fractional crystallization and/or crustal assimilation of the continental crust by under-plating dioritic magma. The higher Al_2O_3/TiO_2 enrichment and the shift from metaluminous to peraluminous in the monzogranite suggest a longer residence time within the continental crust, during which fractional crystallization and the assimilation of pre-existing crustal components into the dioritic magma that resulted in the formation of the monzogranite. The study requires replication at other areas within the basin to generate enough data to enhance metallogenic studies in the terrain.

KEYWORDS

Magma differentiation, Fractional crystallization, Crustal assimilation, Peraluminous, Geotectonic setting.

1. INTRODUCTION

The southern portion of the West African Craton (WAC), referred to as the Leo-Man Shield consists of crystalline basement rocks of Archean age in the west and the Birimian crystalline basement rocks of Paleoproterozoic age in the east (Figure 1).
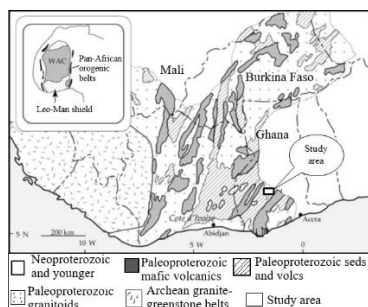
Figure 1: Geological map of the Leo-Man shield showing the study site (Attoh et al., 2006).

The Birimian rocks were formed during a period of accretion of island arcs from 2.1 Ga to 2.0 Ga (Hirdes et al., 1992). Some researchers proposed that the Birimian was formed during the Eburnean orogeny from 2.27 to 1.98 Ga (Taylor et al., 1988; Abouchami et al., 1990). This age also accounted for the emplacement and deformation of syn- to post-orogenic granitoids that are related to extensive metallogenic activities involving the placement of gold (Abouchami et al., 1990; Leube et al., 1990; Feybesse et al., 2006). Metamorphic grade ranges from greenschist to amphibolite facies (Oberthür et al., 1998; Eisenlohr and Hirdes, 1992).

Some researchers are of the view that the Birimian crust formed as an oceanic plateau in association with plume activity, while others suggested a major crust-forming event that is associated with extensive juvenile magmatism in an intra-oceanic setting from 2.35 to 1.98 Ga (Abouchami et al., 1990; Boher et al., 1992; Taylor et al., 1992; Feybesse et al., 1990). The Birimian terrain is characterized by structural and compositional variations of geologic formations that occur as alternating greenstone belts and metasedimentary basins (Abouchami et al., 1990; Davis et al., 1994).

The evolution of magmas and the associated geodynamics in continental settings are normally complex because of crustal contamination and

Quick Response Code	Access this article online	
	Website: www.earthsciencesmalaysia.com	**DOI:** 10.26480/esmy.02.2020.118.126

fractional crystallization, which may mask the source characteristics of the geologic formations (Essaifi and Zayane, 2018). According to some researchers, masking of geologic formations is evident by the wide variations in chemical composition and isotopic signatures of the continental intraplate basalts from Ocean Island basalts and the continental crust (Wilson, 1993; Ma et al., 2013). Tracing the source of the intraplate continental magmatism, therefore, requires knowledge of the interactive history of the magmas of the lithospheric mantle and the continental crust during evolution and emplacement (Essaifi and Zayane, 2018).

The Birimian granitoids consist of two main types; the older I-type and the younger S-type. It is postulated that the I-type is related to subduction processes or basal melting of thick oceanic plateau, while the S-type is related to intracrustal melting (Doumbia et al., 1998; Hirdes et al., 2002; Feybesse et al., 2006; Leube et al., 1990; Hirdes et al., 1992; Sylvester and Attoh, 1992 and Abouchami et al., 1990). Some researchers suggested that the granitoid suites are coeval, (Taylor et al., 1988; 1992), while others are of the view that the belt-type granitoid is older by about 60-90 Ma (Hirdes et al., 1992). The belt-type granitoid (I-type) occurs predominantly in greenstone belts, while the basin-type granitoid (S-type) occur mainly in metasedimentary basins (Eisenlohr and Hirdes, 1992; Feybesse et al., 2006).

In Ghana, the belt-type granitoids have been extensively studied when compared to the basin-type granitoids, probably due to a perceived higher metallogenic potential associated with the belt-type granitoids (Davis et al., 1994; Hirdes et al., 1992; 1996; Loh and Hirdes, 1999). This perception is however changing in recent years due to the discovery of a 10-20 km wide shear zone that dissects the Kumasi basin. This shear zone is characterised by reactivated thrust faults that supports hydrothermal fluid flow and gold mineralisation (Chudasama et al., 2016). The above development is very important since increased geological studies in the basins will generate enough data for comparison with the belt zones to better understand the metallogenic history of the entire Birimian terrain.

On the regional scale, the general Birimian terrain remains classified as alternating sedimentary basins and volcanic greenstone belts, associated syn- to post-orogenic granitoids (Abouchami et al., 1990; Leube et al., 1990; Hirdes et al., 1996; Doumbia et al., 1998). The greenstone belts are overlain by clastic sediments of the Tarkwaian group (Leube et al., 1990; Taylor et al., 1992; Hirdes et al., 1992). The metasedimentary basins consist of felsic to intermediate volcaniclastic and sedimentary rocks (Abouchami et al., 1990; Leube et al., 1990).

The belt-type granitoids constitute relatively small intrusive bodies that are medium-grained and homogeneous (Doumbia et al., 1998; de Kock et al., 2011). The rocks are mainly metaluminous and relatively Na-rich hornblende to biotite-bearing granodiorite to diorite, monzonite and syenite suites (Perrouty et al., 2012; Block et al., 2015; McFarlane et al., 2019). The basin-type granitoids also consist of coarse-grained large batholiths and are commonly associated with transcurrent faults, heterogeneous with migmatitic textures, and quartz veins and pegmatite (Feybesse et al., 2006). The rocks are predominantly peraluminous and relatively Ca-rich and include biotite and muscovite granites and granodiorites (Eisenlohr and Hirdes, 1992).

The Kumasi Basin lies between the Ashanti greenstone belt in the southeast and Sefwi–Bibiani greenstone belt in the northwest, with deep-seated fault zones (Agyei-Duodu et al., 2009; Perrouty et al., 2012). The basin developed between 2150 Ma and 2100 Ma, initially as a foreland basin, consisting of "flysch-like" metasedimentary rocks that were derived from the adjacent greenstone belts (Davis et al., 1994; Jessell et al., 2012). Over time, the Basin evolved into a back-arc basin that was subducted beneath active volcanic arcs (Chudasama et al., 2016). Ongoing thinning of the crust triggered asthenospheric upwelling with evolution of a mantle plume causing underplating of the thinned crust by mafic magmas (Siddorn and Lee, 2005).

The resultant intermediate to felsic peraluminous melts produced in the lower crust were emplaced in the upper crust as plutons (Chudasama et al., 2016). The peraluminous character and abundance of muscovite and biotite in the plutonic suite are interpreted as evidence for the assimilation of the continental crust into the upwelling, plume-like magma chamber during partial melting. Eventually, the entire Birimian sequence was uplifted and eroded during the Eburnean orogeny (Taylor et al., 1988; Leube et al., 1990; Hirdes et al., 1996; Oberthür et al., 1998; Hirdes and Davis, 2002).

The area under study lies at the north-eastern margin of the intra-basin

Asankrangwa shear that dissects the Kumasi basin, and is hence perceived to have a major influence on the characteristics of the granitoids, which may require a reappraisal for further classifications. This research investigates the petrological and geochemical characteristics of some granitoids sampled from the northern part of the Kumasi basin in Ghana with the aim of classifying them appropriately to establish the origin of the magmas as well as their geodynamic setting.

2. MATERIALS AND METHODS

2.1 Study site and Sampling

The study area is situated between Longitude 1°19'57"-1°24'54" W and Latitude 6°45'15"- 6° 50'12" N in the north-eastern part of the Ashanti region in southern Ghana (Figure 1). During field work, three types of granitoid intrusive rocks were identified; these are quartz diorite, granodiorite, and monzogranite. Five representative samples from each type of granitoids were collected and prepared for thin sections and whole-rock geochemical analysis. Sample locations are shown in Figure 2.
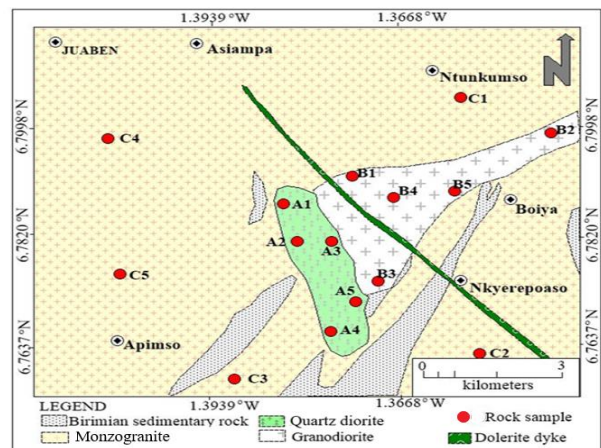
Figure 2: Geological map of the study area (after Agyei-Duodu et al, 2009).

2.2 Petrographic study and modal analysis

The samples were cleaned and then cut for thin section preparation. A grinding machine and corundum dust were used to smoothen and flatten the surface of the rock slabs. The sample chip was fixed to the frosted side of a glass slide using epoxy and then grounded to a constant thickness of 30um. A coverslip was added to protect the thin section from damage and to increase clarity in the microscope. The thin sections were studied using a polarized light microscope to identify mineral components. The granitoids occurring in the study area were classified using the Streckeisen modal QAP (quartz, alkali feldspar and plagioclase) classification scheme (Streckeisen, 1979).

2.3 Geochemical Analysis

Whole rock geochemical analysis of the selected samples was done at Australian Laboratory Services (ALS), Canada. The inductively coupled mass spectrometer (ICP-MS) was employed to analyze for the rare earth and minor/trace elemental compositions of the samples. The ICP-MS hydride generation method was used according to procedural descriptions (Skoog et al., 2007). Major element compositions were analysed on the X-ray fluorescence spectrometer (SPECTRO X-LAB2000). About 4.0 g of pulverized rock samples were weighed and blended for 3 minutes and pressed into pellets for analyses. As a check for accuracy, fused discs were prepared following procedures described and used for the analysis of one-third of the total samples (Wirth and Barth, 2016). The reason for cross-checking with the fused disc is that common errors may occur with both methods during sample preparation, calibration curve settings and equipment configuration.

For example, in pressed pellets, platy minerals cover more areas and cause heterogeneous surfaces, leading to matrix effects of auto-absorption of X-rays by irradiated samples, while the fused discs provide homogenous samples and eliminate matrix effect. The results from both procedures were indistinguishable (Wirth and Barth, 2016). Geochemical classification of the granitoids was done using the Geochemical Data Toolkit Version 4.00 (Janoušek et al., 2006).

3. RESULTS

3.1 Field observation and petrographic analysis

Representative photographs of outcrops and photomicrographs of thin sections for the three types of granitoids recognized in this study are shown in Figure 3. The quartz diorite (Figure 3A, B) is mesocratic, medium to coarse-grained and exhibits hypidiomorphic and porphyritic textures with laths of clouded plagioclase feldspar. The plagioclase phenocrysts show poikilitic or sieve textures due to the inclusions of quartz, biotite and amphibole. The hornblende crystals are euhedral and exhibit very feeble pleochroic colours that range from bottle green to greenish-yellow. Microcline shows cross-hatched twinning and is anhedral-subhedral, while quartz has irregular shapes. Biotite is mottled with perfect cleavage.

Figure 3: (A, C and E): Field photographs of the quatz diorite, granodiorite and monzogranite and photomicrographs (B, D and F) of same under crossed polarized light x40.

Hbl=hornblende, Pl=plagioclase, Qz=quartz, Bt=Biotite, Grt=Garnet, Mc=microcline, K-feld=potash feldspar (Whitney and Evans, 2010)

The granodiorite (Figure 3C, D) is light to dark-grey, coarse-grained with hypidiomorphic texture and composed of quartz, plagioclase feldspar, muscovite and garnet. Calcic plagioclase constitutes more than two-thirds of the total feldspars in all the thin sections. Potash feldspars are mostly microcline with distinctive tartan twinning. The accessory mineral garnet is euhedral with a well-preserved hexagonal shape and characteristic isotropic nature. Muscovite is anhedral, tabular and sparsely distributed with a preferred orientation, and mostly occur at quartz-plagioclase boundaries.

The monzogranite (Figure 3E, F) is pinkish-grey, coarse-grained and quartz-veined. It is composed of phenocrysts of plagioclase and microcline exhibiting feeble cross-hatched twinning. Flakes of biotite occur marginal to microcline and have pleochroic colours that range from brown to greenish-yellow. Plagioclase is very subordinate with polysynthetic twinning characteristics. Quartz minerals are irregular in shape sometimes showing yellowish and bluish interference colours with inclusions of feldspars and biotite. The opaque minerals are also irregular, forming sutured boundaries with other minerals. Biotite shows slight evidence of alteration to chlorite. The chlorite shows green absorption and high interference colours. The average modal values estimated for the minerals identified are presented in Table 1, while the QAP plot is presented in Figure 4.

Table 1: Average modal composition in percent of the analyzed granitoids.

Sample	Qz	Pl	K-feld	Iron oxide	Bt	Opq	Hbl	Ms	Grt
Quartz diorite	10-15	45-55	2-10	1-2	2-8	1-2	15-25	1-2	-
Granodiorite	30-35	35-45	5-10	1-2	5-10	<1	5-10	8-10	<1
Monzogranite	50-60	8-10	20-25	1-2	8-12	<1	-	2-4	-
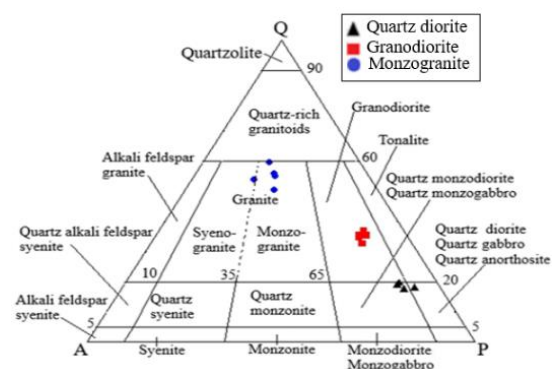
Figure 4: QAP diagram of the granitoids sampled (Streckeisen, 1979)

3.2 Geochemical analysis

Major elements, trace elements, rare earth elements and normalisation data for the analyzed samples are presented in Tables 2, 3 and 4

Table 2: Chemical analysis of major elements (wt.%), trace elements (ppm) and rare earth elements (REEs) of the analyzed granitoids															
	Quartz diorite					Granodiorite					Monzogranite				
Major Oxides	A1	A2	A3	A4	A5	B1	B2	B3	B4	B5	C1	C2	C3	C4	C5
SiO$_2$	61.64	61.22	59.87	59.96	61.32	66.41	68.25	66.16	68.54	66.20	69.38	69.79	72.93	73.01	70.93
TiO$_2$	0.91	0.47	0.81	1.17	0.85	0.53	0.24	0.42	0.42	0.47	0.01	0.01	0.14	0.01	0.01
Al$_2$O$_3$	15.29	14.59	12.00	13.57	14.39	15.30	15.40	16.14	15.16	15.50	16.81	17.19	16.70	16.68	16.32
Fe$_2$O$_3$	7.18	4.89	9.36	8.24	4.44	4.72	3.71	4.25	4.15	4.66	0.63	0.41	0.62	0.46	0.34
MnO	0.03	0.05	0.09	0.05	0.09	0.05	0.03	0.06	0.06	0.07	0.03	0.03	0.04	0.06	0.09
MgO	3.71	4.37	7.82	6.83	4.22	2.52	2.10	2.91	1.66	2.56	1.03	0.82	0.32	0.03	0.65
CaO	6.45	7.74	6.65	6.64	7.44	4.33	3.94	4.27	4.41	4.52	2.36	2.29	2.46	2.29	2.32
Na$_2$O	3.11	4.21	2.60	3.03	4.11	3.59	4.23	3.57	4.05	4.10	5.16	4.95	3.71	5.35	5.24
K$_2$O	1.49	1.39	0.53	1.01	1.69	2.22	2.03	2.46	2.28	2.70	3.96	3.72	2.63	2.26	2.83
P$_2$O$_5$	0.43	0.49	0.90	0.34	0.85	0.12	0.34	0.22	0.14	0.12	0.10	0.07	0.64	0.30	0.34
SO$_3$	0.02	0.02	0.05	0.12	0.27	0.24	0.07	0.06	0.07	0.04	0.01	0.01	0.01	0.01	0.01
Total	100.26	99.44	100.68	100.96	99.67	100.03	100.34	100.52	100.94	100.94	99.48	99.29	100.20	100.46	99.08
Trace Elements															
Ag	0.09	0.06	0.10	0.10	0.05	0.06	0.04	0.07	0.06	0.06	0.02	0.01	0.01	0.02	0.01
As	0.19	0.19	0.19	0.19	0.19	0.50	0.19	0.19	0.29	0.24	0.19	0.19	0.19	0.19	0.19
Ge	0.24	0.16	0.25	0.23	0.26	0.14	0.13	0.15	0.14	0.15	0.05	0.05	0.09	0.05	0.05
In	0.07	0.03	0.08	0.10	0.03	0.03	0.03	0.04	0.03	0.03	0.01	0.01	0.03	0.01	0.00
Cd	0.10	0.05	0.09	0.10	0.04	0.04	0.08	0.06	0.06	0.06	0.03	0.03	0.02	0.05	0.04
Co	22.20	14.60	49.70	30.90	13.90	12.90	2.80	18.20	11.30	14.75	0.40	0.20	2.10	0.20	0.80
Bi	0.09	0.04	0.13	0.07	0.03	0.06	0.33	0.06	0.15	0.11	2.10	1.22	0.17	0.96	0.25
Cr	140.00	116.00	403.00	198.00	114.00	88.00	16.00	148.00	84.00	116.00	3.00	5.00	16.00	10.00	8.00
Ta	0.38	0.27	0.08	0.19	0.23	0.15	0.30	0.31	0.25	0.28	1.06	1.17	2.10	1.38	1.19
Te	0.04	0.04	0.04	0.04	0.04	0.04	0.04	0.04	0.04	0.04	0.04	0.04	0.04	0.04	0.04
Tl	0.48	0.26	0.20	0.18	0.23	0.33	1.15	0.81	0.76	0.79	1.33	1.83	1.07	2.10	2.05
U	1.10	0.80	0.50	0.60	0.60	0.30	5.10	0.50	1.97	1.23	3.60	3.00	2.90	8.90	7.56
V	134.00	84.00	234.00	185.00	82.00	86.00	15.00	85.00	62.00	73.50	1.00	0.90	15.00	1.00	1.00
Cu	29.00	11.20	60.70	37.30	10.90	19.40	1.50	16.90	12.60	14.75	3.10	1.10	4.50	0.90	0.80
Be	1.12	1.01	0.83	0.89	1.01	0.31	3.31	3.00	2.21	2.60	5.04	6.39	8.80	6.41	6.80
Cs	14.15	4.39	28.30	8.15	4.32	17.45	11.55	42.80	23.93	33.37	12.90	8.33	13.80	12.80	10.70
Ga	21.00	20.60	17.00	21.80	21.20	15.40	30.30	21.50	22.40	21.95	26.50	22.50	40.50	28.60	26.50
Ba	340.00	470.00	130.00	350.00	465.00	380.00	560.00	580.00	506.67	543.33	30.00	10.00	240.00	10.00	24.00
Li	500.00	156.50	353.00	354.00	130.50	470.00	345.00	800.00	538.33	669.17	135.50	53.40	260.00	89.50	78.70
Mo	0.42	0.31	0.23	0.34	0.41	0.48	0.50	0.54	0.51	0.52	0.25	0.28	0.53	0.69	0.55
Nb	5.50	3.90	2.00	4.20	5.30	3.50	3.70	4.00	3.73	3.87	8.20	5.40	11.40	7.40	6.80
Ni	70.10	44.40	300.00	108.00	42.80	32.90	4.60	73.00	36.83	54.92	1.40	0.90	4.90	1.10	1.50
Pb	6.80	7.20	3.40	4.30	6.90	6.40	19.90	7.30	11.20	9.25	20.50	21.20	8.00	16.40	14.23
Rb	61.30	35.90	33.80	23.70	33.87	74.80	239.00	87.00	133.60	110.30	261.00	351.00	281.00	387.00	346.00
Sb	0.07	0.09	0.06	0.09	0.08	0.07	0.05	0.05	0.06	0.05	0.05	0.05	0.05	0.06	0.05
Sc	19.00	13.30	37.40	29.00	12.60	14.30	3.30	12.90	10.17	11.53	0.40	0.30	3.10	0.40	0.30
Se	2.00	1.00	2.00	2.00	1.00	1.00	1.00	1.00	1.00	1.00	1.00	1.00	0.90	1.00	1.00
Sn	2.40	0.90	1.90	1.00	0.70	1.20	4.40	4.00	3.20	3.60	6.80	8.10	24.00	11.40	10.60
Sr	686.00	586.00	381.00	609.00	568.00	553.00	197.00	532.00	427.33	479.67	239.10	252.70	223.00	177.87	296.40
W	0.20	0.10	0.20	0.30	0.09	0.10	0.30	0.10	0.17	0.13	0.20	0.20	0.60	0.20	0.20
Th	2.10	1.80	0.60	1.10	1.40	1.00	7.20	0.80	3.00	1.90	0.70	0.50	5.60	0.90	5.60
Zr	44.80	49.60	43.10	46.20	45.60	44.00	106.50	85.20	78.57	81.88	26.10	27.60	79.40	46.00	44.40
Hf	1.90	1.70	1.70	1.80	1.80	1.10	3.00	2.30	2.13	2.22	1.40	1.70	2.60	2.40	2.20
Zn	78.00	66.00	83.00	78.00	64.00	46.00	55.00	77.00	59.33	68.17	26.00	20.00	60.00	24.00	22.00
Y	24.2	9.9	19.9	25.7	9.7	5.60	4.70	7.20	5.83	6.52	1.90	2.00	5.40	2.90	2.84
REEs															
La	18.50	10.10	9.40	9.10	9.91	10.80	17.50	4.80	11.03	7.92	1.60	1.20	12.00	1.20	1.90
Ce	49.90	25.40	27.30	26.80	20.40	21.60	38.80	12.80	24.40	18.60	3.12	2.59	26.60	2.65	2.36
Pr	7.25	3.18	4.50	4.53	3.08	2.48	4.77	1.46	2.90	2.18	0.32	0.31	3.20	0.28	0.25
Nd	30.80	12.90	21.50	22.30	10.50	9.00	17.40	6.00	10.80	8.40	0.90	1.20	11.60	0.80	0.77
Sm	5.98	2.51	4.95	5.66	2.31	1.69	3.19	1.31	2.06	1.69	0.23	0.26	2.08	0.19	0.15
Eu	1.84	1.04	1.86	1.92	1.02	1.10	0.64	0.87	0.87	0.87	0.04	0.07	0.36	0.02	0.02
Gd	5.55	2.46	5.28	6.13	2.28	1.91	2.40	1.53	1.95	1.74	0.20	0.23	1.51	0.20	0.20
Tb	0.86	0.38	0.81	0.97	0.32	0.28	0.27	0.26	0.27	0.27	0.05	0.04	0.20	0.06	0.04
Dy	4.29	1.79	4.02	4.89	1.59	1.21	0.90	1.35	1.15	1.25	0.25	0.22	0.81	0.32	0.29
Ho	0.95	0.40	0.87	1.08	0.20	0.25	0.16	0.31	0.24	0.28	0.05	0.04	0.15	0.07	0.06
Er	2.69	1.12	2.35	2.88	1.09	0.70	0.37	0.90	0.66	0.78	0.15	0.14	0.40	0.23	0.19
Tm	0.36	0.15	0.29	0.36	0.20	0.10	0.05	0.12	0.09	0.11	0.02	0.03	0.05	0.04	0.04
Yb	2.32	1.00	1.76	2.24	0.91	0.83	0.30	0.88	0.67	0.78	0.19	0.22	0.35	0.34	0.33
Lu	0.36	0.16	0.26	0.33	0.26	0.14	0.06	0.15	0.12	0.13	0.03	0.03	0.06	0.05	0.05
Total	131.65	62.59	85.15	89.19	54.07	52.09	86.81	32.74	57.21	45.00	7.15	6.58	59.37	6.45	6.65

*A= Quartz diorite B= Granodiorite C= Monzogranite
*Major oxides in Wt. %. Trace elements in ppm

Table 3: Normalized REE (ppm) values of the granitoids sampled

	Quartz diorite					Granodiorite					monzogranite				
Norm REE	A1	A2	A3	A4	A5	B1	B2	B3	B4	B5	C1	C2	C3	C4	C5
LaN	59.68	32.58	30.32	29.35	31.97	34.84	56.45	15.48	35.58	25.55	5.16	3.87	38.71	3.87	6.13
CeN	61.76	31.44	33.79	33.17	25.25	26.73	48.02	15.84	30.20	23.02	3.86	3.21	32.92	3.28	2.92
PrN	59.43	26.07	36.89	37.13	25.25	20.33	39.10	11.97	23.77	17.87	2.62	2.54	26.23	2.30	2.05
NdN	51.33	21.50	35.83	37.17	17.50	15.00	29.00	10.00	18.00	14.00	1.50	2.00	19.33	1.33	1.28
SmN	30.67	12.87	25.38	29.03	11.85	8.67	16.36	6.72	10.56	8.67	1.18	1.33	10.67	0.97	0.77
EuN	25.03	14.15	25.31	26.12	13.88	14.97	8.71	11.84	11.84	11.84	0.54	0.95	4.90	0.27	0.27
GdN	21.43	9.50	20.39	23.67	8.80	7.37	9.27	5.91	7.53	6.72	0.77	0.89	5.83	0.77	0.77
TbN	18.14	8.02	17.09	20.46	6.75	5.91	5.70	5.49	5.70	5.70	1.05	0.84	4.22	1.27	0.84
DyN	13.31	5.56	12.48	15.18	4.93	3.76	2.79	4.19	3.57	3.88	0.78	0.68	2.51	0.99	0.90
HoN	13.23	5.57	12.12	15.04	2.79	3.48	2.23	4.32	3.34	3.90	0.70	0.56	2.09	0.97	0.84
ErN	12.81	5.33	11.19	13.71	5.19	3.33	1.76	4.29	3.14	3.71	0.71	0.67	1.90	1.10	0.90
TmN	11.11	4.63	8.95	11.11	6.17	3.09	1.54	3.70	2.78	3.40	0.62	0.93	1.54	1.23	1.23
YbN	11.10	4.78	8.42	10.72	4.35	3.97	1.44	4.21	3.21	3.73	0.91	1.05	1.67	1.63	1.58
LuN	11.18	4.97	8.07	10.25	8.07	4.35	1.86	4.66	3.73	4.04	0.93	0.93	1.86	1.55	1.55

Table 4: Selected REE (ppm) ratios of the granitoids sampled

Rock type	Eu/Eu*	(La/Yb)$_N$	(Gd/Yb)$_N$	(La/Sm)$_N$	K$_2$O/Na$_2$O	(Nb/La)$_{PM}$	(Th/U)$_{PM}$	(Ce/Pb)$_{PM}$	REE $_{(tot)}$
Quartz diorite	1.15	5.17	2.11	1.88	0.35	0.36	0.58	0.47	422.65
Granodiorite	1.47	13.94	2.77	3.22	0.60	0.36	0.38	0.19	273.85
Monzogranite	0.55	7.75	1.23	4.57	0.64	2.16	0.13	0.04	86.20

A subscript 'N' indicates normalization to chondrite values after Boynton, (1984). Likewise, a subscript 'PM' represents normalization to the primitive mantle after McDonough and Sun, (1995). Also, A/CNK is the molar [Al_2O_3/ ($CaO+Na_2O+K_2O$)] whilst Eu-anomalies (Eu/Eu*) were calculated using the formula [$EuN/\sqrt{SmN*GdN}$].

3.3 Petrographic study

From the petrographic analysis (Table 1), the average modal estimations for the quartz diorite are 10-15% quartz, 45-55% plagioclase feldspar, and 2-10% alkali feldspar. The average modal estimations for the granodiorite show 30-35% quartz, 35-45% plagioclase feldspar, and 5-10% alkali feldspar. The monzogranite contains 50-60% quartz, 8-10% plagioclase feldspar, and 20-25% alkali feldspar. Furthermore, the plots of all the samples on the QAP ternary diagram in Figure 4 are in agreement with our field descriptions and petrographic analysis of quartz diorite, granodiorite and monzogranite.

3.4 Major elements

In the Total-Alkali Silica (TAS) diagram (Figure 5), the quartz diorite samples plot in the diorite field. The granodiorite samples plot in the granodiorite field while the monzogranite samples plot in the field of granite.
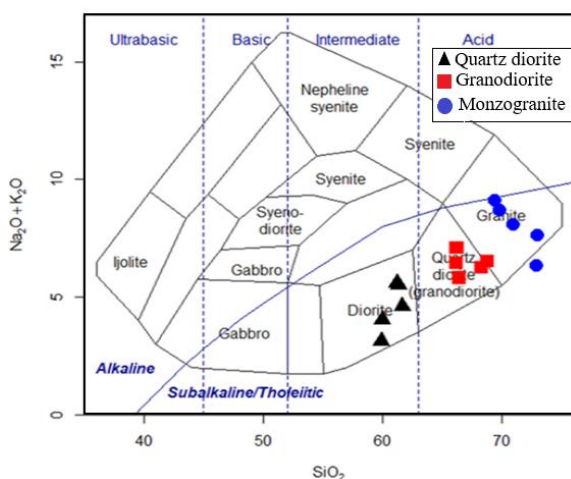
Figure 5: Total Alkaline Silica (TAS) diagram: Na_2O+K_2O against SiO_2 (Cox et al, 1979)

These results show consistency between the petrographic and geochemical analyses, attesting to the unaltered nature of the rock samples used for this study. Generally, SiO_2 contents of all three granitoids sampled range from 59.87-73.01 wt. %. Conversely, the Fe_2O_3+MgO contents established from this study is 6.23-8.67 wt. %. The K_2O/Na_2O ratio for the quartz diorite, granodiorite and monzogranite are 0.35, 0.60 and 0.64 respectively. The low values of K_2O/Na_2O ratio suggest minute occurrence of K-bearing minerals such as K-feldspar, muscovite and biotite (McLennan et al., 1983; Osae et al., 2006). Harker diagrams were used to establish the magma differentiation processes based on the variation in the concentration of the major oxides against SiO_2 for the three categories of samples (Figure 6).
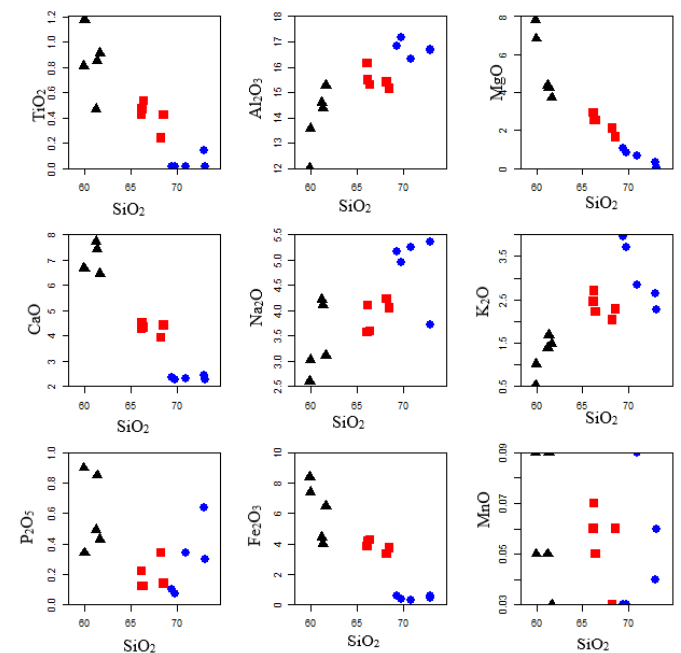
Figure 6: Harker diagrams showing variations of major oxides with silica. (Black triangle = quartz diorite, red square = granodiorite, blue circle = monzogranite)

In Figure 6, major oxides of the quartz diorite correlate weakly with SiO_2. The overall decreasing trend of Fe_2O_3, MnO, TiO_2 and MgO in the quartz diorite may suggest high fractionation of mafic minerals like biotite or hornblende (Nyarko et al., 2012). In addition, Al_2O_3, TiO_2, K_2O, MgO, and MnO in the granodiorites also display slightly decreasing trends with SiO_2 which may indicate the fractionation of plagioclase, apatite, titanite, biotite and hornblende during the crystallization.

In the monzogranites, Fe_2O_3, Na_2O, TiO_2, MgO and CaO exhibit slightly positive correlation with SiO_2, which probably indicate the removal of the oxides from the melt as a result of fractional crystallization. The magma differentiation process was further studied with the Total alkali+Fe_2O_3+MgO (AFM) diagram in Figure 7 and showed that all the rock types show linear trends as well as calc-alkaline affinity.
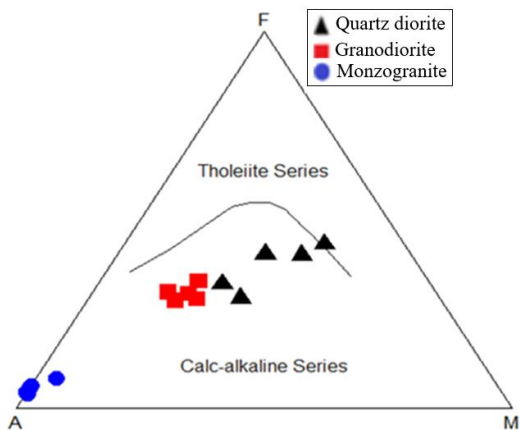
Figure 7: AFM (A=Na$_2$O + K$_2$O), F=Fe$_2$O$_3$, M=MgO) diagram, showing a Calc-alkaline affinity for the rocks. The Calc-alkaline and tholeiitic series differentiation line (Irvine and Barager, 1971).

In Figure 7, the monzogranites display a high alkali affinity, while the quartz diorites show comparatively low alkali affinity. The K-affinity is low, medium and medium-high for the quartz diorite, granodiorite and monzogranite samples, respectively (Figure 8A), while the A/CNK-A/NK diagram (Figure 8B) shows that the quartz diorite and granodiorite samples are metaluminous grading into peralumimous character for the monzogranites.
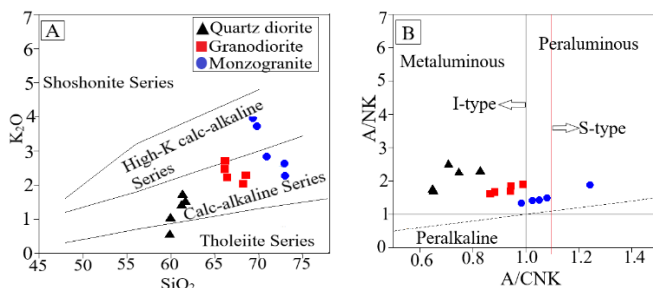
Figure 8: (A) The K$_2$O vs SiO$_2$ diagram after Peccerillo and Taylor, indicates a medium to High- K affinity of the granitoids (Peccerillo and Taylor, 1976). (B) The plot of alumina saturation vs alkalinity of the granitoids showing majority of the samples within the I-type and one fall in the s-type granite field (Maniar and Piccoli, 1989; Chappell and White, 1974).

3.5   Trace and rare earth element composition

The Primitive mantle and chondrite normalised (spider) plots established, respectively, were used to constrain the environment of magma generation and the extent of crustal contamination, if any, in the magma or melt, leading to the production of the studied granitoid suite (McDonough and Sun, 1995; Boynton, 1984).
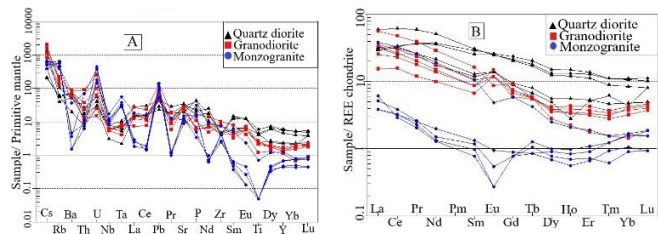
Figure 9: Multi-element plots explaining magma source and differentiation (A) Primitive mantle spider plot normalized and (B) REE Chondrite spider plot after (McDonough and Sun, 1995; Boynton, 1984)

In the normalized primitive mantle spider diagram in Figure 9A, most of the samples show similar distribution patterns. They generally demonstrate enrichments in the large ion lithophile elements (LILEs) such as Rb, Ba, Sr, and Th, as well as the light rare earth elements (LREEs). La,

Ce, Pr, Nd, Sm and the high field strength elements (HFSE) Nb, Ta, and Zr, while, the heavy rare earth elements (HREEs) Eu, Dy, Yb and Lu are depleted and portray a flat distribution pattern, and display negative Ti anomalies.

In the quartz diorite, a trough is observed at La-Ce and a negative anomaly at Ti. The quartz diorite has an average Eu/Eu* of 1.15, (La/Yb) $_N$ of 5.17, (Gd/Yb) $_N$ of 2.11, (La/Sm) $_N$ of 1.88. Similarly, the granodiorite also shows a trough at Nb-Ta and a slight negative anomaly at Ti. Besides, the granodiorite has an average Eu/Eu* of 1.47, (La/Yb) $_N$ of 13.97, (Gd/Yb) $_N$ of 2.77 and (La/Sm) $_N$ of 3.22. For the monzogranite, a trough is observed at Ta-Ce and negative Rb, Nd, Eu and Ti anomalies. They also have an average Eu/Eu* of 0.55, (La/Yb) $_N$ of 7.75, (Gd/Yb) $_N$ of 1.23 and (La/Sm) $_N$ of 4.57.

In the REE chondrite spider plot in Figure 9B, virtually all the samples show LREE enrichments and generally flat HREEs. The HREEs in the monzogranite samples are slightly depleted than the other two granitoids and exhibits a negative Eu anomaly. The ∑REE concentrations decrease from the quartz diorite (422.65 ppm), through granodiorite (273.85 ppm) to monzogranite (86.20ppm). Thus, the quartz diorites and granodiorite samples show enrichments in the ∑REEs compared to the monzogranites. However, the quartz diorite has an average (Nb/La) $_{PM}$ of 0.36, (Th/U) $_{PM}$ of 0.58, and (Ce/Pb) $_{PM}$ of 0.47. The granodiorite has an average (Nb/La) $_{PM}$ of 0.36, (Th/U) $_{PM}$ of 0.38, and (Ce/Pb) $_{PM}$ of 0.19 and the monzogranite has an average (Nb/La) $_{PM}$ of 2.16, (Th/U) $_{PM}$ of 0.13, (Ce/Pb) $_{PM}$ of 0.04. The tectonic settings of the granitoids were estimated as presented in Figure 10 (Pearce et al., 1984).
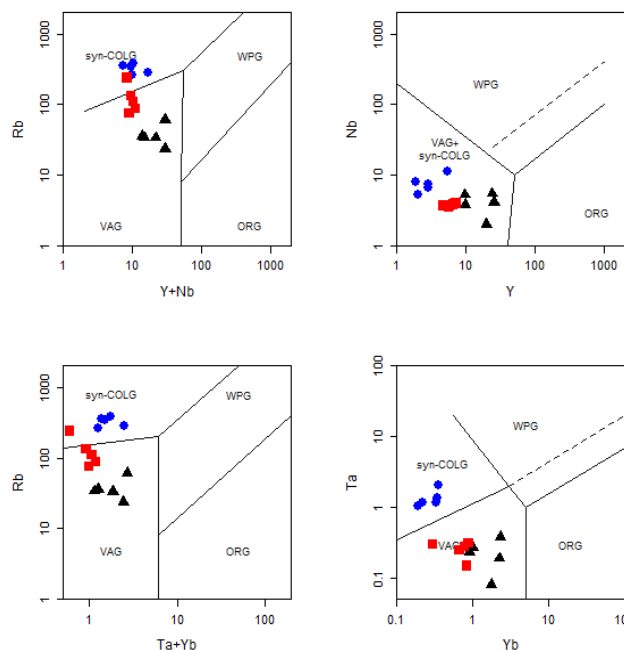
Figure 10: Tectonic discrimination diagram for the basin type granitoids of the North Eastern margin of the Kumasi basin: Rb versus Y+Nb, Rb versus Ta+Yb, Ta versus Yb and Nb versus Y (Pearce et al., 1984). The granitoids show VAG and Syn-COLG affinity (Black triangle = quartz diorite, red square = granodiorite, blue circle = monzogranite).

From Figure 10, the quartz diorite and granodiorite plot in the volcanic arc granite (VAG) field while the monzogranites plot in the syn collisional granite (syn-COLG) field. In the Nb/Y diagram, all the samples for each rock type plot in the VAG + syn-COLG field.

4.   DISCUSSION

4.1   Petrogenesis and tectonic implication

The differences in the geochemical compositions of the granitoid suites in the Kumasi basin suggest that the rocks were generated by different processes and from different sources (Tando et al., 2016). However, our results show that in this part of the Kumasi Basin, a common magmatic source for all the rock types is indicated by the linear trends of major oxides and trace elements in the Harker-type diagrams (Figures 6 and 9) and the similarity in the distribution patterns of the incompatible elements (REEs, LILEs and HFSEs). However the suite of different

granitoid rocks resulted from processes of magma differentiation and/or partial melting at various stages of the magma evolution as done (Leube et al., 1990).

Magma differentiation and the fractionation of plagioclase and pyroxene can easily explain the linear trends of major oxides and trace elements. On the other hand, residual effects of partial melting, fractional crystallization and/or crustal assimilation are noted, such as depletion in incompatible elements: the highest ∑REE concentrations are registered in the quartz diorites, which decreases through granodiorite to the lowest ∑REE concentrations in the monzogranite.

Concentration of potassium and the Al_2O_3/Na_2O ratio are important petrogenetic indicators of crustal assimilation by magmatic systems that underplate the lower crust. The low K_2O concentration of the quartz diorite suggests minimal crustal assimilation during magma underplating of the lower crust. On the other hand, both granodiorite and monzogranite exhibited same amounts and range of K_2O enrichment relative to that of the quartz diorite (Figure 8A). These K_2O enrichments suggest that the granodiorite and monzogranite were formed from fractional crystallization and/or crustal assimilation of the continental crust by the underplating dioritic magma.

The wide variation in the K_2O concentrations in quartz diorite (0.53 wt %-1.69 wt %), granodiorite (2.03 wt %-2.70 wt %), monzogranite (2.26 wt %-3.96 wt %) buttresses the fact that the granodiorite and monzogranite comprise some more fractionated minerals and/or assimilated crust in comparison to the quartz diorite. The higher Al_2O_3/TiO_2 enrichment and the shift to peraluminous character in the monzogranite compared to the metaluminous granodiorite (Figure 8B) suggests longer residence time within the continental crust, during which fractional crystallization and assimilation of crustal components into the dioritic magma resulted in the formation of the monzogranites in the Kumasi Basin.

4.2 Geodynamics of the granitoids based on the Kumasi Basin geology

Extensive geological, geophysical and structural studies conducted by various researchers on the Kumasi Basin suggest that it was initially a foreland basin that eventually rifted apart in a back arc-style to form a series of horst-graben structures (e.g. Feybesse et al., 2006; Chudasama et al., 2016). These structures created a basin-like feature that accommodated and accumulated eroded volcaniclastics from the fault-bounded Birrimian volcanic belts to the east (Ashanti Belt) and west (Sefwi-Bibiani Belt), thereby, creating the appearance of a thick continental supracrustal unit. The rifting and push against the volcanic belts might have influenced the nature of sheared contacts between the Kumasi Basin and these two fault-bounding volcanic belts. There is so far no clear evidence that the Belt volcanics subducted under the Kumasi Basin (Feybesse et al., 2006; Chudasama et al., 2016).

Our results for the granitoids show that, relative to adjacent elements in geochemical arrays of primitive-mantle-normalized multi-element diagrams, Sr, Ba and K are consistently enriched, while Rb, Nb, and Ti are depleted (Figure 9A). The enrichment patterns in LILEs and depletion in HFSEs appear to corroborate with a calc-alkaline nature shown in Figures (7 and 9) for the studied granitoids; features that are characteristic of hydrous arc magmatism and mostly restricted to subduction-related plate tectonic processes, as shown in Figure 10 (Winter, 2001). However, these processes are not in agreement with the basin structure of the Kumasi Basin and its contact relationship with the Volcanic Belts. This, therefore, negates the possibility of dehydration of subducted mafic crust beneath the Kumasi Basin to generate the observed hydrous magma characteristics exhibited by the studied granitoids.

On the other hand, combining the distribution patterns of incompatible elements (high LREEs and flat HREEs; high LILEs and low HFSEs contents) and the relatively positive Eu/Eu*anomalies exhibited by quartz diorite (Eu/Eu*=1.15) and granodiorite (Eu/Eu*=1.47), we suggest that the quartz diorite and granodiorite originated from melts that formed in a water-saturated (hydrous) environment where the stability of plagioclase was suppressed against the hydrous minerals and that the negative Eu/Eu* anomaly exhibited by the monzogranite indicate fractionation of plagioclase in the final stages of the magma evolution (Tarney and Jones, 1994). In particular, we propose that in this section of the Kumasi Basin, the water-rich environment was not derived from dehydration of hydrous minerals under subduction zone (arc) magmatism but rather from the dewatering of foreland volcaniclastic sediments within the Kumasi Basin during regional subsidence, burial, and metamorphism.

Foreland basin sediments are host to abundant water within their pore spaces. The rifting of the Kumasi Basin further implies that the dioritic magma was generated by "plume-like" magmatism that underplated the lower crust (Feybesse et al., 2006; Chudasama et al., 2016). This underplating resulted in the partial melting to form the granodioritic magma in the upper crust. However, given the expansive distribution of the monzogranite relative to the other two granitoid bodies (Figure 2), the bulk of the evolved magma underwent a longer residence time in the upper crust that allowed for the gradual assimilation of crustal rocks of the Kumasi Basin to form the monzogranitic rocks.

As stated above, supported by the similar range in amounts of K_2O enrichment with the granodiorites but high Al_2O_3/TiO_2 ratios, decrease in incompatible elements and the shift from metaluminous to peraluminous characteristics relative to the quartz diorite and granodiorite. Again, all of these characteristics imply that fractional crystallization and a gradual assimilation of crustal components of pre-existing Basin rocks resulted in the progressive evolution of a juvenile mafic magma from quartz diorite through granodiorite to monzogranite in the north-eastern part of the Kumasi Basin.

5. Conclusion and Recommendations

The granitoids in the study area have a common source; however, processes of magma differentiation and/or partial melting at various stages of the magma evolution probably resulted in the different granitoid suites. The quartz diorite and granodiorite originated from melts that formed in a water-saturated environment, while the monzogranite partly formed during the fractionation of plagioclase in the final stages of the magma evolution. The granodiorite and monzogranite formed from fractional crystallization and/or crustal assimilation of the continental crust by the under-plating dioritic magma. The basin-type granitoids in this study exhibited I-type signatures, which is uncommon and must be taken into account when studying their petrogenesis and tectonic settings in geological re-construction studies, in order not to misinterpret their environment of formation. It is recommended that similar work be done on the granitoids occurring at the middle and southern parts of the Kumasi basin to establish a more comprehensive database that can help to further understand the petrogenesis of these granitoids, as well as the metallurgic patterns to enhance exploration activities.

References

Abouchami, W., Boher, M., Michard, A., Albarède, F., 1990. A major 2.1 Ga event of mantle magmatism in West Africa: An early stage of crustal accretion. Journal of Geophysical Research, 95, Pp. 17605–17629

Adadey, K., Clarke, B., Théveniaut, H., Urien, P., Delor, C., Roig, J.Y., Feybesse, J.L., 2009. Geological map explanation - Map sheet 0503 B (1:100 000), CGS/BRGM/Geoman, Geological Survey Department of Ghana (GSD). No MSSP/2005/GSD/5a

Agyei-Duodu, J., Loh, G.K., Boamah, K.O., Baba, M., Hirdes, W., Toloczyki, M. and Davis, D.W., 2009. Geological map of Ghana 1:1 000 000. Geological Survey Department of Ghana.

Attoh, K., Evans, M.J., Bickford, M.E., 2006. Geochemistry of an ultramafic rodingite rock association in the Paleoproterozoic Dixcove greenstone belt, southwestern Ghana. Journal of African Earth Sciences, 45, Pp. 333–346.

Block, S., Ganne, J., Baratoux, L., Zeh, A., Parra-Avila, A.L., Jessell, M., Ailleres, L., and Siebenaller, L., 2015. Petrological and geochronological constraints on lower crust exhumation during Paleoproterozoic (Eburnean) orogeny, NW Ghana, West African craton. J. Metamorph Geol., 33, Pp. 463–494.

Boher, M., Abouchami, W., Michard, A., Albarède, F., Arndt, N.T., 1992. Crustal growth in West Africa at 2.1 Ga. Journal of Geophysical Research, 97, Pp. 345-369.

Bonhomme, M., 1962. Contribution à l'étude géochronologique de la plate-forme de l'Ouest africain. Imprimerie Louis-Jean.

Boynton, W.V., 1984. Cosmochemistry of the rare earth elements: meteorite studies. Rare earth element geochemistry, Ed. by P. Henderson (Elsevier, Amsterdam), Pp. 63–114.

Chappell, B.W., White, A.J.R., 1974. Two contrasting granite types. Pac. Geol., 8, Pp. 173-174.

Chudasama, B., Porwal, A., Kreuzer, O.P., Butera, K., 2016. Geology, geodynamics and orogenic gold prospectivity modelling of the Paleoproterozoic Kumasi Basin, Ghana, West Africa, Ore Geology Review: http://dx.doi.org/10.1016/

Cox, K.G., Bell, J.D., Pankhurst, R.J., 1979. The Interpretation of Igneous Rocks. London (George Allen & Unwin), xiv + 450, Pp. 197.

Davis, D., Hirdes, W., Schellenger, E., Nunoo, E.A., 1994. U/Pb age constraints on deposition and provenance of Birimian and gold-bearing Tarkwaian sediments in Ghana, West Africa. Precambrian Research, 130, Pp. 113-137.

de Kock, G.S., Armstrong, R.A., Siegfried, H.P., Thomas, E., 2011. Geochronology of the Birimian Supergroup of the West African craton in the Wa-Bolé region of west-central Ghana: Implications for the stratigraphic framework. Journal of African Earth Sciences, 59, Pp. 1-40.

Doumbia, S., Pouclet, A., Kouamelan, A., Peucat, J.J., Vidal, M., Delor, C., 1998. Petrogenesis of juvenile-type Birimian (Paleoproterozoic) granitoids in central Côte d 'Ivoire, West Africa: geochemistry and geochronology. Precambrian Research, 87, Pp. 33-63.

Eisenlohr, B.N., Hirdes, W., 1992. The structural development of the early Proterozoic Birimian and Tarkwaian rocks of southwest Ghana, West Africa. Journal of African Earth Sciences, 14, Pp. 313-325.

Essaifi, A., Zayane, R., 2018. Petrogenesis and origin of the Upper Jurassic-Lower Cretaceous magmatism in Central High Atlas (Morocco): Major, Trace element and Isotopic (Sr-Nd) constraints: Journal of African Earth Sciences, 137, Pp. 229e245.

Feybesse, J.L., Billa, M., Guerrot, C., Duguey, E., Lescuyer, J.L., Milési, J.P., Bouchot, V., 2006. The Paleoproterozoic Ghanaian province: geodynamic model and ore controls, including regional stress modelling. Precambrian Research, 149, Pp. 149–196.

Ghana. SRK Consulting Report No. SRK 2CP005.000/001 (70 pp.). Hall.

Hirdes, W., Davis, D.W., Eisenlohr, B.N., 1992. Reassessment of Proterozoic granitoids ages in Ghana on the basis of U/Pb Zircons and Monazite dating. Precambrian Research, 56, Pp. 889-96.

Hirdes, W., Davis, D.W., Lüdtke, G., Konan, G. 1996. Two generations of Birimian (Paleoproterozoic) volcanic belts in northeastern Côte d'Ivoire (West Africa), as demonstrated by precise U–Pb mineral dating: Consequences for 'Birimian Controversy'. Precambrian Research, 80, Pp. 173–199.

Irvine, T.N., Baragar, W.R.A., 1971. A guide to the chemical classification of the common volcanic rocks. Canadian Journal of Earth Sciences, 8, Pp. 523-548.

Janoušek, V., Farrow, C.M., Erban, V., 2006. Interpretation of Whole-rock Geochemical Data in Igneous Geochemistry: Introducing Geochemical Data Toolkit (GCDkit). Journal of Petrology, 47, Pp. 1255–1259. https://doi.org/10.1093/petrology/egl013

Jessell, M.W., Amponsah, P.O., Baratoux, L., Asiedu, D.K., Loh, G.K., Ganne, J., 2012. Crustal-scale transcurrent shearing in the paleoproterozoic Sefwi-Sunyani-Comoe region, West Africa. Precambrian Research, 212, Pp. 155-168.

Leube, A., Hirdes, W., Mauer, R., Kesse, G.O., 1990. The early Proterozoic Birimian Supergroup of Ghana and some aspects of its associated gold mineralization. Precambrian Research., Pp. 46-165.

Loh, G., Hirdes, W., 1999. Explanatory notes for the geological map of Southwest Ghana 1:100000: Sekondi (0402A) and Axim (0403B) sheets. Ghana Geological Survey Bulletin, 49, Pp. 1-149.

Ma, G.S.K., Malpas, J., Suzuki, K., Lo, C.H., Wang, K.L., Iizuka, Y., Xenophontos, C., 2013. Evolution and origin of the Miocene intraplate basalts on the Aleppo plateau, NW Syria. Chemical Geology, 335, Pp. 149e171.

Maniar, P.D., Piccoli, P.M., 1989. Tectonic discrimination of granitoids. Geological Society of American Bulletin, 101, Pp. 635-643.

McDonough, W.F., Sun, S.S., 1995. The composition of the earth. Chemical Geology, 120, Pp. 23e253.

McFarlane, H.B., Ailleres, L., Betts, P., Ganne, J., Baratoux, L., Jessell, M.W., Block, S., 2019. Episodic collisional orogenesis and lower crust exhumation during the Palaeoproterozoic Eburnean Orogeny: Evidence from the Sefwi Greenstone Belt, West African Craton. Precambr. Res., 325, Pp. 88–110.

McLennan, S.M., Taylor, S.R., Eriksson, K.A., 1983. Geochemistry of Archaean shales from Pilbara Supergroup, Western Australia. Geochim. Cosmochim. Acta, 47, Pp. 1211–1222.

Nyarko, S.E., Asiedu, D.K., Dampare, S., 2012. Estimation of Temperature, Pressure and Oxygen Fugacity of the Cal-Alkaline Basin-Type Granitoids in the Winneba Area, Ghana. Research Journal of Environmental and Earth Sciences, 4(1), Pp. 41-47.

Oberthür, T., Vetter, U., Davis, D.W., Amanor, J.A., 1998. Age constraints on gold mineralization and Paleoproterozoic crustal evolution in the Ashanti belt of Southern Ghana. Precambrian Res., 89, Pp. 129-143.

Osae, S., Asiedu, D.K., Banoeng-Yakubo, B., Koeberl, C., Dampare, S.B., 2006. Provenance and tectonic setting of Late Proterozoic Buem sandstones of southeastern Ghana: Evidence from geochemistry and detrital modes. J. Afr. Earth Sci., 44, Pp. 85- 96.

Pearce, J.A., Harris, N.B.W., Tindle, A.G., 1984. Trace element discrimination diagrams for the interpretation of granitic rocks. Journal of petrology, 25, Pp. 956–983.

Peccerilo, A., Taylor, S.R., 1976. Geochemistry of Eocene calc-alkaline volcanic rocks from Kastamonu area, Northern Turkey. Contributions to Mineralogy and Petrology, 58, Pp. 63-81.

Perrouty, S., Ailleres, L., Jessell, M.W., Baratoux, L., Bourassa, Y., Crawford, B., 2012. Revised Eburnearn geodynamic evolution of the gold-rich southern Ashanti Belt, Ghana, with new field and geophysical evidence of the pre-Tarkwaian deformations. PrecambrianRes, 204–205, Pp. 12–39.

Siddorn, J., Lee, C., 2005. Structural geology of the Ashanti II concessions, Southwest

Skoog, D.A., Holler, F.J., Crouch, S.R., 2007. Principles of Instrumental Analysis. Thomson Higher Education.

Streckeisen, A., Le Maitre, R.W.A., 1979. Chemical approximation to the modal QAPF classification of the igneous rocks. Egypt Neues Jahrb Mineral Abh, 136, Pp. 169-206.

Sylvester, P.J., Attoh, K., 1992. Lithostratigraphy and composition of 2.1 Ga greenstone belts of the West African Craton and their bearing on crustal evolution and Archean-Proterozoic boundary. J. of Geol., 100, Pp. 377-393.

Tandoh, K.K., Morgan, A., Seckley, A.W., Brako, B.A., 2016. Geochemical characteristics of the basin-type granitoids in the Atia and its surrounding areas of Kumasi basin of Ghana. Int. Journal of Scientific & Eng. Research, 7(12).

Tarney, J., Jones, C.E., 1994. Trace element geochemistry of orogenic igneous rocks and crustal growth models. Journal of the Geological Society, 151(5), Pp. 855-868.

Taylor, P.N., Moorbath, S., Leube, A., Hirdes, W., 1988. Geochronology and Crustal Evolution of Early Proterozoic Granite-Greenstone Terrains in Ghana, West Africa: In International Conference and Workshop on the Geology of Ghana with Special Emphasis on Gold: Programme and Abstracts, Accra, Ghana, Pp. 43-45.

Taylor, P.N., Moorbath, S., Leube, A., Hirdes, W., 1992. Early Proterozoic crustal evolution in the Birimian of Ghana, Constraints from geochronology and isotope geochemistry. Precambrian Research, 56, Pp. 97-111.

Taylor, S.R., McLennan, S.M., 1985. The continental crust: Its composition and evolution. Blackwell Scientific Publications, Oxford, Pp. 1–312.

Whitney, D.L., Evans, B.W., 2010. Abbreviations for names of rock-forming minerals. American mineralogist, 95(1), Pp. 185.

Wilson, M., 1993. Geochemical Signatures of Continental and Oceanic Basalts: a Key to Mantle Dynamics? Journal of Geological Society of London, 150, Pp. 977e990.

Winter, J.D., 2001. An introduction to Igneous and Metamorphic Petrology. Prentice.

Wirth, K., Barth, A., 2016. Geochemical Instrumentation and Analysis (XRF).